A phase-field regularized cohesive zone model for hydrogen assisted cracking

Jian-Ying Wu[a,*], Tushar Kanti Mandal[b], Vinh Phu Nguyen[b]

[a] *State Key Laboratory of Subtropical Building Science, South China University of Technology, 510641 Guangzhou, China*
[b] *Department of Civil Engineering, Monash University, Clayton, Victoria 3800, Australia*

Abstract

Being able to seamlessly deal with complex crack patterns like branching, merging and even fragmentation, phase-field fracture/damage models are promising in the modeling of localized failure in solids. This paper addresses a phase-field regularized cohesive zone model (PF-CZM) for hydrogen assisted cracking based on our previous work on purely mechanical problems. Two distinct hydrogen enhanced decohesion mechanisms are dealt with by introducing various implicitly defined (via the crack phase-field) hydrogen-dependent softening laws. The resulting models are then numerically tested and compared against several benchmark examples. It is found that, though the PF-CZM gives different results regarding various decohesion mechanisms, the global responses are insensitive to both the mesh discretization resolution and the incorporated length scale parameter even in the presence of hydrogen.

1. Introduction

Within the context of continuum mechanics [1] – which seems more convenient for structural analysis – this paper presents a new phase-field damage/fracture model for hydrogen assisted cracking (HAC). HAC or hydrogen embrittlement is a form of material degradation that occurs in metals due to the presence of atomic hydrogen. Susceptibility to HAC is often a result of the introduction of hydrogen during coating, forming, plating, and finishing operations, often referred to as *internal embrittlement*. Hydrogen may also be introduced over time – the so-called *external embrittlement* – through environmental exposure, corrosion processes, cathodic protection, etc. When hydrogen is present, metallic materials often fail at a much lower load level than that can be sustained under a hydrogen-free environment. This usually results in catastrophic failure which occurs unexpectedly, sometimes suddenly after many years of service, severely threatening the life-cycle safety of metallic structures.

One premise of HAC is the localization of hydrogen atoms that occurs at hot spots around dislocations, grain boundaries, interfaces between different phases, voids or cracks. The transport of hydrogen can be modeled by a diffusion process, thus resulting in a coupled displacement–hydrogen concentration problem for HAC; see the

---

* Corresponding author.
  E-mail address: jywu@scut.edu.cn (J.-Y. Wu).

seminal work presented in [2–5] and [6] among many others. It is now a common consensus that [6–8] two failure mechanisms are responsible for hydrogen embrittlement, i.e., the hydrogen enhanced localized plasticity (HELP) in which hydrogen favors the mobility of dislocations or local plasticity even if there is a macroscopically brittle failure, and the hydrogen enhanced decohesion (HEDE) in which interstitial hydrogen lowers the cohesive strength. Though the former can be incorporated as in [9], only the latter HEDE is considered in this work.

In the literature, the HEDE mechanism is usually modeled using the cohesive zone model (CZM) of Barenblatt [10] with a hydrogen-dependent fracture energy [11–14]. As cracks are treated using zero-thickness interface elements (see e.g., [15,16] and [17]), only a limited set of cracks along inter-element boundaries is allowed. Intra-element crack paths can be captured either by the embedded strong discontinuity approach [18,19] or by the extended finite element method [20,21]. However, despite the noteworthy recent contributions [22–25], it is still a challenging issue for these CZM based discontinuous methods to model complex fracture problems that involve multiple intersecting cracks [26,27], needless saying their applications to HAC.

Comparatively, in phase-field models for fracture/damage [28,29], referred to as PFMs hereafter, one does not need *ad hoc* failure criteria to determine when/where a crack nucleates, how much and along which direction it propagates. In PFMs, a scalar field, i.e., the crack phase-field, is introduced to blend sharp cracks and the intact bulk, resulting in a diffuse damage band of which the bandwidth is controlled by a length scale parameter. Being able to model fracture with complex crack paths over a fixed mesh, PFMs have been applied to brittle fracture [30–32], ductile fracture [33–35], dynamic fracture [36–40], cohesive fracture [41–46], and multi-physics fracture [47–51]. We refer to Bourdin et al. [52], Ambati et al. [53] and Wu et al. [54] for the comprehensive reviews.

PFMs have also been employed to model HAC using a hydrogen-dependent (decreasing) fracture energy [9,55–57]. Even though good results have been reported [55,56], all the previous studies rely on the standard PFM of Bourdin et al. [29] and Miehe et al. [58] for brittle fracture that suffers from the following drawbacks: *(i)* cohesive fracture is not considered, *(ii)* different degradation responses, in which hydrogen reduces the fracture energy and/or cohesive strength, are not dealt with.

Regarding the above facts, the objective of this work is to extend our previous phase-field regularized cohesive zone model [32,41,42], or shortly, PF-CZM, to the problem of hydrogen assisted cracking. Developed within the unified phase-field theory [41], the PF-CZM applies to both brittle and cohesive fracture, and its response is insensitive to the length scale parameter [32,42,43]. Motivated by the CZM based discontinuous approach for HAC [4], we employ implicitly defined (via the crack phase-field) hydrogen-dependent softening laws. Regarding degradation of the cohesive (failure) strength and fracture energy, two models with distinct HEDE mechanisms are proposed. Several numerical examples of varying complexities are provided to demonstrate their performances.

The remainder of this paper is organized as follows. Section 2 briefly recalls our phase-field regularized cohesive zone model for purely mechanical problems. Its extension to hydrogen assisted cracking is addressed in Section 3. The representative examples are presented in Section 4. The relevant conclusions are drawn in Section 5.

Notation. Compact tensor notation is used in this paper. As general rules, scalars are denoted by italic light-face Greek or Latin letters (e.g. a or λ); vectors, second- and fourth-order tensors are signified by italic boldface minuscule, majuscule and blackboard-bold majuscule characters like $\boldsymbol{a}$, $\boldsymbol{A}$ and $\mathbb{A}$, respectively. The inner products with single and double contractions are denoted by '·' and ':', respectively.

2. The phase-field regularized cohesive zone model (PF-CZM) for purely mechanical problems

As the PF-CZM for purely mechanical problems has been extensively addressed in our previous publications [32, 41,42], only the fundamental formulation is recalled in this section.

As shown in Fig. 1(a), the reference configuration of a cracking solid $\Omega \subset \mathbb{R}^{n_{\dim}}$ ($n_{\dim} = 1, 2, 3$) with a sharp crack/interface set $\mathcal{S} \subset \mathbb{R}^{n_{\dim}-1}$ is considered. The external boundary is denoted by $\partial\Omega \subset \mathbb{R}^{n_{\dim}-1}$, with $\boldsymbol{n}$ being the outward unit normal vector. The material particles are labeled by their spatial coordinates $\boldsymbol{x}$. The solid is kinematically characterized by the displacement field $\boldsymbol{u}(\boldsymbol{x}, t) : \Omega \times [0, T] \rightarrow \mathbb{R}^{n_{\dim}}$ in time $t \in [0, T] \in \mathbb{R}_+$ for some time interval $T > 0$. Upon the assumption of infinitesimal deformations, the strain field $\boldsymbol{\epsilon}(\boldsymbol{x}, t) : \Omega \times [0, T] \rightarrow [\mathbb{R}^{n_{\dim} \times n_{\dim}}]^{\text{sym}}$ is given by $\boldsymbol{\epsilon}(\boldsymbol{x}, t) := \nabla^{\text{sym}}\boldsymbol{u}(\boldsymbol{x}, t)$, for the symmetric gradient operator $\nabla^{\text{sym}}(\cdot)$ with respect to the spatial coordinates $\boldsymbol{x}$. Assume the solid is subjected to specific volumetric body forces (per unit mass) $\boldsymbol{b}^*(\boldsymbol{x}, t) : \Omega \times [0, T] \rightarrow \mathbb{R}^{n_{\dim}}$ and surface boundary tractions $\boldsymbol{t}^*(\boldsymbol{x}, t) : \partial\Omega_t \times [0, T] \rightarrow \mathbb{R}^{n_{\dim}-1}$ for some part of the external boundary $\partial\Omega_t \subseteq \partial\Omega$. Given displacements $\boldsymbol{u}^* : \partial\Omega_u \times [0, T] \rightarrow \mathbb{R}^{n_{\dim}}$ are applied to the disjoint remaining boundary $\partial\Omega_u \subseteq \partial\Omega$.

Components	Governing equations	Constitutive relations	Characteristic functions
Displacement sub-problem	$\begin{cases} \nabla \cdot \boldsymbol{\sigma} + \boldsymbol{b}^* = \boldsymbol{0} \\ \boldsymbol{\sigma} \cdot \boldsymbol{n} = \boldsymbol{t}^* \end{cases}$	$\begin{cases} \boldsymbol{\sigma} = \omega(d)\mathbb{E}_0 : \boldsymbol{\epsilon} \\ Y = -\omega'(d)\bar{Y} \end{cases}$	$\begin{cases} \omega(d) = \dfrac{(1-d)^p}{(1-d)^p + a_1 \cdot P(d)} \\ P(d) = 1 + a_2 d + a_3 d^2 + \cdots \end{cases}$
Damage sub-problem[a]	$\begin{cases} \nabla \cdot \boldsymbol{q} + Q(d) \leq 0 \\ \boldsymbol{q} \cdot \boldsymbol{n}_{\mathcal{B}} \geq 0 \end{cases}$	$\begin{cases} \boldsymbol{q} = \dfrac{2b}{c_\alpha} G_{\mathrm{f}} \cdot \nabla d \\ Q = Y - \dfrac{G_{\mathrm{f}}}{c_\alpha b} \alpha'(d) \end{cases}$	$\begin{cases} \alpha(d) = 1 - (1-d)^2 \\ c_\alpha = 4 \displaystyle\int_0^1 \sqrt{\alpha(\beta)}\, d\beta = \pi \end{cases}$
Model parameters	$a_1 = \dfrac{4}{\pi}\dfrac{l_{\mathrm{ch}}}{b}$	$a_2 = 2\beta_k^{\frac{2}{3}} - \left(p + \dfrac{1}{2}\right)$	$a_3 = \begin{cases} 0 & p > 2 \\ \dfrac{1}{2}\beta_w^2 - (1 + a_2) & p = 2 \end{cases}$

[a]The conditions $\dot{d} \geq 0$ and $d \in [0, 1]$ have to be fulfilled; b is a length scale parameter that can be taken as small as possible.

Box I. The phase-field regularized cohesive zone model (PF-CZM) for purely mechanical problems.

Within the framework of PFMs [29,41,42,52,59], the sharp crack or interface $\mathcal{S}$ is smeared over the localization band $\mathcal{B} \subseteq \Omega$ in which the so-called crack phase-field or damage field $d(\boldsymbol{x}, T) : \mathcal{B} \times [0, T] \to [0, 1]$ localizes, with the exterior domain $\Omega \backslash \mathcal{B}$ being intact; see Fig. 1(b). Note that the localization band $\mathcal{B}$ is usually a much smaller sub-domain. As in the classical continuum damage mechanics, $d(\boldsymbol{x}) = 0$ means intact material with no damage whereas $d(\boldsymbol{x}) = 1$ represents complete fracture.

In accordance with [32,41,42], the PF-CZM for purely mechanical problems is summarized in Box I.

In the above box, the effective damage driving force $\bar{Y} := \frac{1}{2}\bar{\sigma}_{\mathrm{eq}}^2/E_0$ is defined in terms of an equivalent effective stress $\bar{\sigma}_{\mathrm{eq}}$, with E_0 being Young's modulus. For brittle and quasi-brittle fracture, the classical Rankine criterion can be adopted, i.e., $\bar{\sigma}_{\mathrm{eq}} = \langle \bar{\sigma}_1 \rangle$, where $\bar{\sigma}_1$ denotes the major principal value of the effective stress tensor $\bar{\boldsymbol{\sigma}} := \mathbb{E}_0 : \boldsymbol{\epsilon}$, with $\mathbb{E}_0$ being the fourth-order elasticity tensor. Irwin's internal length is defined as $l_{\mathrm{ch}} := E_0 G_{\mathrm{f}}/f_{\mathrm{t}}^2$, with f_{t} and G_{f} being the failure strength and fracture energy (toughness), respectively. Ratios β_k and β_w compare the initial slope k_0 and the limit crack opening w_c of the target traction–separation law (TSL) to those of the linear TSL, i.e.,

$$\beta_k := \frac{k_0}{-\frac{1}{2}f_{\mathrm{t}}^2/G_{\mathrm{f}}} \geq 1, \qquad \beta_w := \frac{w_c}{2G_{\mathrm{f}}/f_{\mathrm{t}}} \tag{2.1}$$

Consequently, the resulting parameters a_2 and a_3 depend only on the specific softening curve. For instance, regarding the linear and exponential softening curves it follows that [41,42,44]

$$\begin{cases} \text{Linear softening curve:} & p = 2.0, \ a_2 = -\frac{1}{2}, & a_3 = 0 \\ \text{Exponential softening curve:} & p = 2.5, \ a_2 = 2^{5/3} - 3, & a_3 = 0 \end{cases} \tag{2.2}$$

The resulting softening curves are compared in Fig. 2 against the analytical ones.

Remark 2.1. The above PF-CZM needs the following parameters: Young's modulus E_0, Poisson's ratio ν_0, the fracture toughness G_{f}, the tensile strength f_{t} and an appropriate softening law (which gives the exponent p and parameters a_2 and a_3). Provided the length scale parameter b is sufficiently small compared to the characteristic dimension of structures, it has negligible effects on the crack pattern and global response [32,41–43]. Therefore, it is always possible to select a sufficiently small b to have Γ-convergence to sharp cracks. For other phase-field models, the length scale has to be a material parameter [31,60,61] which can be too large to yield narrow bands mimicking sharp cracks; see [54]. $\square$

Remark 2.2. Similarly to the discontinuous CZM, the above PF-CZM applies to both brittle and cohesive fracture. In particular, for a material with very large failure strength f_{t} but very small fracture energy G_{f}, Irwin's length scale l_{ch} approaches zero and the PF-CZM asymptotically converges to Griffith's brittle fracture theory [32]. $\square$
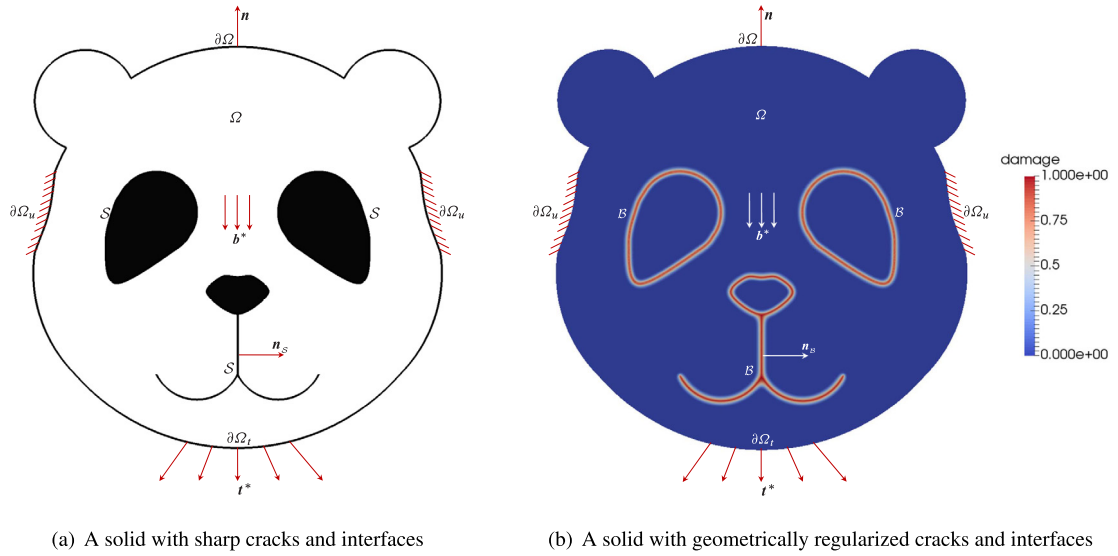
(a) A solid with sharp cracks and interfaces   (b) A solid with geometrically regularized cracks and interfaces

Fig. 1. A cracking solid with sharp cracks/interfaces and the geometric regularization.

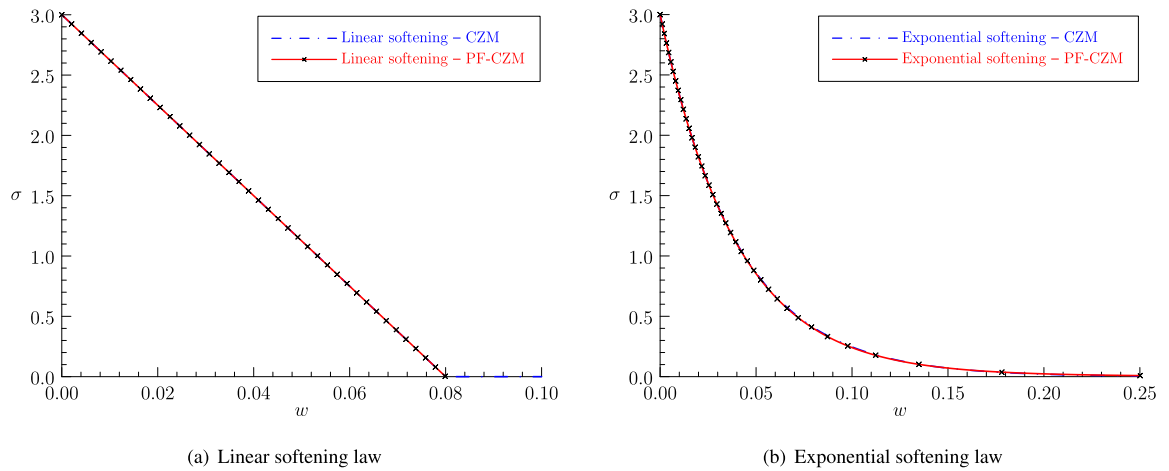(a) Linear softening law   (b) Exponential softening law

Fig. 2. The target softening curves and phase-field approximations ($f_t = 3.0$ MPa, $G_f = 0.12$ N/mm).

3. The PF-CZM for hydrogen assisted cracking

In this section, the above PF-CZM is extended to incorporate the effect of hydrogen assisted cracking. In particular, two models with distinct HEDE mechanisms are proposed.

3.1. Mass diffusion of hydrogen

For the hydrogen diffusion, the governing equation reads

$$\begin{cases} \dot{C} = -\nabla \cdot \boldsymbol{J} & \text{in } \Omega \\ \boldsymbol{J} \cdot \boldsymbol{n} = J^* & \text{on } \partial\Omega_J \end{cases} \tag{3.1}$$

for the prescribed hydrogen flux J^* on the part $\partial\Omega_J$ of the boundary $\partial\Omega$; see Remark 3.1 for the Dirichlet boundary conditions (BCs).

In accordance with Fick's law, the flux $\boldsymbol{J}$ is given by [62]

$$\boldsymbol{J} = -\frac{DC}{RT}\nabla\mu = -D\nabla C + \frac{DV_{\mathrm{H}}}{RT}C\nabla\sigma_{\mathrm{H}} \tag{3.2}$$

for the following molar bulk chemical potential μ of the impurity [4]

$$\mu = \mu_0(T) + RT\ln C - V_{\mathrm{H}}\sigma_{\mathrm{H}} \tag{3.3}$$

where D is the bulk diffusivity, C is the bulk hydrogen concentration, $R = 8.314$ J/(mol K) is the universal gas constant, T is the absolute temperature, V_{H} is the partial molar volume of the impurity and $\sigma_{\mathrm{H}} := \frac{1}{3}\mathrm{tr}\boldsymbol{\sigma}$ is the hydrostatic stress; see Remark 3.2.

Remark 3.1. In solving the governing equation (3.1) one also needs the Dirichlet BCs on which the concentration is prescribed, i.e.,

$$C(\boldsymbol{x}, t) = C^* \qquad \text{on } \partial\Omega_C \tag{3.4}$$

for the prescribed hydrogen concentration C^* on the boundary $\partial\Omega_C := \partial\Omega\backslash\partial\Omega_J$. In the literature the following two cases are usually considered

$$C^* = \begin{cases} C^* & \text{(constant Dirichlet BCs)} \\ C^*\exp\left(\dfrac{V_{\mathrm{H}}\sigma_{\mathrm{H}}}{RT}\right) & \text{(stress-dependent Dirichlet BCs)} \end{cases} \tag{3.5}$$

Though the stress-dependent Dirichlet BCs have been used in [4] and [63], the constant Dirichlet BCs are more popular probably due to its easy implementation. □

Remark 3.2. With the flux (3.2), the hydrogen concentration rate becomes

$$\dot{C} = D\Delta C - \frac{DV_{\mathrm{H}}}{RT}\nabla C \cdot \nabla\sigma_{\mathrm{H}} - \frac{DV_{\mathrm{H}}}{RT}C\Delta\sigma_{\mathrm{H}} \tag{3.6}$$

for the Laplacian operator $\Delta(\cdot) = \nabla\cdot\nabla(\cdot)$. Note that sometimes the influence of σ_{H} is neglected as in, e.g., [11,55], resulting in a quite simple equation $\dot{C} = D\Delta C$. □

3.2. Hydrogen-dependent traction–separation laws

In the presence of hydrogen, the material properties decrease with increasing hydrogen concentration. Without loss of generality, let us consider the following generic degradation of the failure strength f_{t} and fracture energy G_{f}

$$f_{\mathrm{t}}(\theta) = \phi_1(\theta)f_{\mathrm{t}0}, \qquad G_{\mathrm{f}}(\theta) = \phi_2(\theta)G_{\mathrm{f}0} \tag{3.7}$$

where the hydrogen degradation functions $\phi_1(\theta)$ and $\phi_2(\theta)$, not necessarily identical, are both expressed in terms of the hydrogen coverage (surface concentration) θ in the cohesive zone; $f_{\mathrm{t}0}$ and $G_{\mathrm{f}0}$ represents the failure strength and fracture energy at null hydrogen concentration (i.e., $\theta = 0$). The explicit expressions of the hydrogen degradation functions will be addressed later in Section 3.3.

For the generic degradation (3.7), Irwin's internal length becomes

$$l_{\mathrm{ch}} := \frac{E_0 G_{\mathrm{f}}}{f_{\mathrm{t}}^2} = \beta_l l_{\mathrm{ch}0} \qquad \text{with} \qquad \beta_l(\theta) = \frac{\phi_2(\theta)}{\phi_1^2(\theta)} \qquad \Longrightarrow \qquad a_1(\theta) = \beta_l(\theta)\frac{4}{\pi}\cdot\frac{l_{\mathrm{ch}0}}{b} \tag{3.8}$$

where $l_{\mathrm{ch}0}$ denotes Irwin's internal length at null hydrogen concentration $\theta = 0$. Note that it is assumed that Young's modulus E_0 is not affected by the hydrogen coverage.

In this work two following particular cases are considered:

- Constant ratio $G_{\mathrm{f}}/f_{\mathrm{t}}$. In this case, both the failure strength and the fracture energy are degraded with the hydrogen coverage θ by an identical monotonically decreasing function $\phi(\theta)$, i.e.,

$$f_{\mathrm{t}}(\theta) = \phi(\theta)f_{\mathrm{t}0}, \qquad G_{\mathrm{f}}(\theta) = \phi(\theta)G_{\mathrm{f}0} \qquad \Longrightarrow \qquad a_1 = \frac{1}{\phi(\theta)}\frac{4l_{\mathrm{ch}0}}{\pi b} \tag{3.9}$$

(a) Linear softening, constant G_f/f_t (Model1)

(b) Exponential softening, constant G_f/f_t (Model1)

(c) Linear softening, constant l_{ch} (Model2)

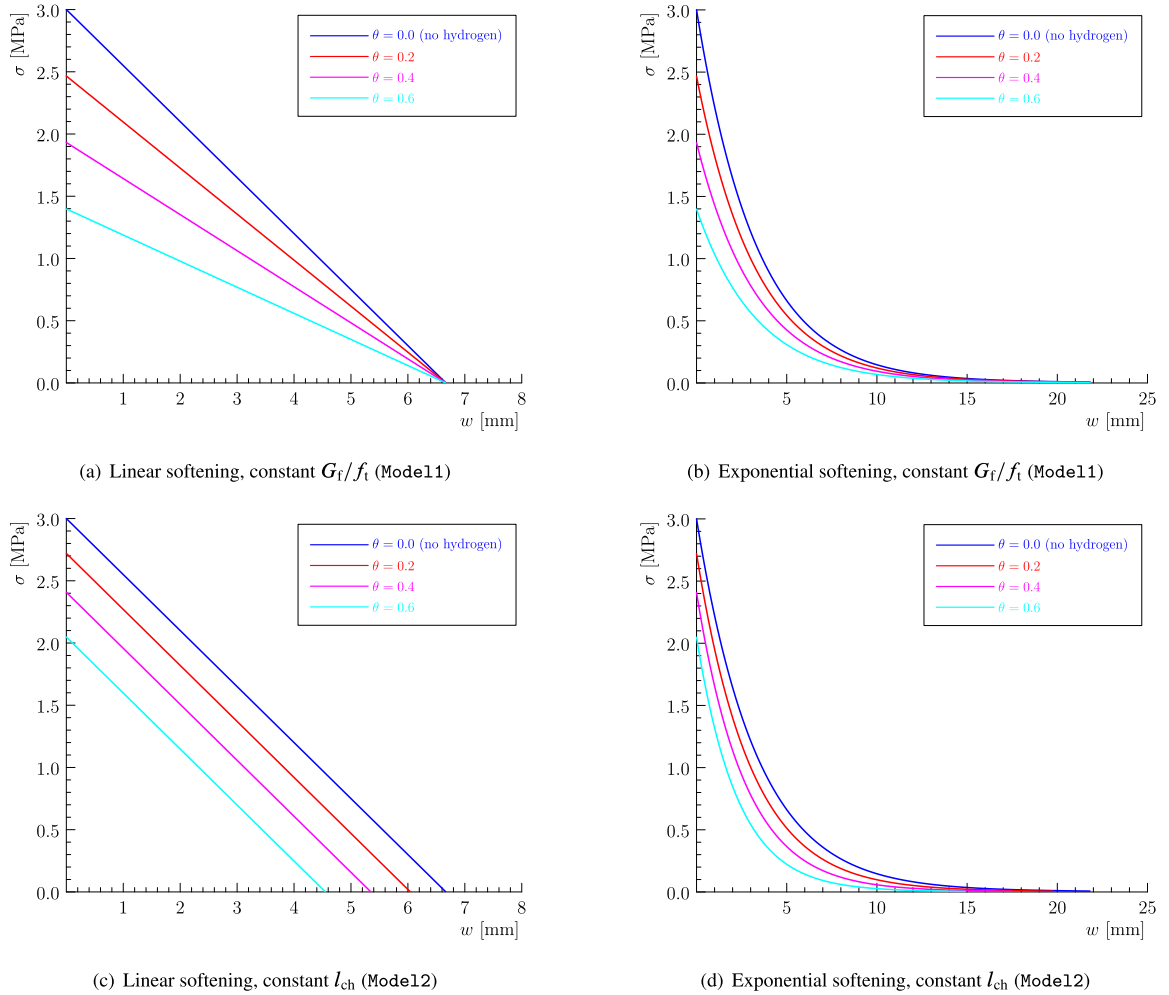(d) Exponential softening, constant l_{ch} (Model2)

Fig. 3. Hydrogen-dependent softening laws with the degradation function (3.15) for $\chi = 0.89$, $G_f = 10$ N/mm and $f_t = 3.0$ MPa.

This choice has been commonly used in the literature [4,5,11,14]. The resulting softening curves resemble those shown in Fig. 3 (a, b). As can be seen, in this case the limit crack opening displacement w_c is kept constant, while Irwin's length scale l_{ch} becomes large with increasing hydrogen concentration. This result is in agreement with the theoretical finding of Lee and Unger [2].

• Constant Irwin's internal length l_{ch}. In [64], it was assumed that the failure strength and the fracture energy are degraded in such a way that Irwin's internal length l_{ch} is fixed, i.e.,

$$f_t(\theta) = \sqrt{\phi(\theta)} f_{t0}, \qquad G_f(\theta) = \phi(\theta) G_{f0} \qquad \Longrightarrow \qquad a_1 = \frac{4l_{ch0}}{\pi b} \tag{3.10}$$

In this case, the parameter a_1 is independent of the hydrogen coverage. The resulting softening curves are shown in Fig. 3 (c, d) in which the limit crack opening w_c also reduces. According to Raykar et al. [64] the degradation in both f_t and w_c is in line with the observed drop in both ultimate strength and percentage elongation of AS-4340 grade after hydrogen embrittlement.

In what follows, Model1 refers to the one with a constant G_f/f_t and Model2 refers to the one with a constant l_{ch}.

Remark 3.3. As in the case of no hydrogen, the ultimate crack band width is given by [41]

$$D_u = b \int_0^1 \alpha^{-1/2}(\beta) \, d\beta \tag{3.11}$$

upon vanishing stress. That is, it depends only on the incorporated length scale parameter b and the adopted geometric crack function $\alpha(d)$, both of which are irrelevant to the hydrogen coverage θ. □

3.3. Hydrogen assisted degradation function

In order to couple the diffusion problem to the PF-CZM with hydrogen-dependent softening laws, one needs to connect the surface concentration θ with the bulk one C. According to Serebrinsky et al. [4], this relation is provided by the Langmuir–McLean isotherm [65]

$$\theta = \frac{C}{C + \exp\left(-\dfrac{\Delta g_b^0}{RT}\right)} \tag{3.12}$$

where C is given in units of impurity mole fraction; Δg_b^0 denotes the Gibbs free energy difference between the adsorbed and bulk standard states. When the bulk concentration C is low, it is usually expressed in the unit of wt. ppm (part per million weight), i.e.,

$$\theta = \frac{5.5 \times 10^{-5} C}{5.5 \times 10^{-5} C + \exp\left(-\dfrac{\Delta g_b^0}{RT}\right)} \tag{3.13}$$

where the coefficient comes from the unit conversion of C from wt. ppm to mole fraction. In the examples presented later in this work, the following parameters are adopted [4,56]: $T = 300$ K, $\Delta g_b^0 = 30$ kJ/mol, $R = 8.314$ J/(mol K), $V_H = 2000$ mm^3/mol unless they are explicitly specified.

In [4], the following quadratic degradation function of the hydrogen coverage was considered

$$\phi(\theta) = 1 - 1.0467\theta + 0.1687\theta^2 \tag{3.14}$$

This dependence was given from first principle calculations. More recently, Martínez-Pañeda et al. [56] proposed using a simpler linear hydrogen-dependent degradation function

$$\phi(\theta) = 1 - \chi\theta \tag{3.15}$$

where the coefficient χ can be estimated by fitting DFT[1] data from the literature. Note that there exist other forms of this hydrogen dependency; see e.g., [11,14] and [55].

Accordingly, using (3.9) and (3.10) together with the degradation function (3.15) one gets the hydrogen-dependent softening curves shown in Fig. 3. As can be seen, the phenomenon of decreasing fracture energy in the presence of hydrogen is captured essentially as those in the discontinuous CZM based approach [4,11,64].

3.4. Governing equations for the coupled mechanical-hydrogen problem

In the proposed multifield problem for HAC, the primary field variables consist of the displacement field $\boldsymbol{u}(\boldsymbol{x}, t)$, the hydrogen concentration field $C(\boldsymbol{x}, t)$ and the damage field $d(\boldsymbol{x}, t)$. The displacement gives the effective crack driving force $\bar{Y}$ (via the strain $\boldsymbol{\epsilon}$) that drives damage evolution and in return, the damage degrades the material properties. The displacement also affects the hydrogen concentration via the hydrostatic stress and in return, the concentration further decreases the material properties. Note that owing to the parameter $a_1(\theta)$ given in Eq. (3.9), for Model1 the mechanical degradation function now depends on both damage and hydrogen (via the coverage θ), i.e., $\omega = \omega(d, C)$.

The governing equations for hydrogen assisted cracking are summarized in Box II.

The above coupled problem can be numerically solved by the multi-field finite element method (FEM). More specifically, the spatial discretization is performed by the standard FEM, with the nodal unknowns consisting

---

[1] Density functional theory is a quantum mechanics based computational method widely used in physics, chemistry and materials science.

Components	Displacement sub-problem	Hydrogen sub-problem	Damage sub-problem[a]
Governing equations	$\begin{cases} \nabla \cdot \boldsymbol{\sigma} + \boldsymbol{b}^* = \boldsymbol{0} \\ \boldsymbol{\sigma} \cdot \boldsymbol{n} = \boldsymbol{t}^* \end{cases}$	$\begin{cases} \nabla \cdot \boldsymbol{J} + \dot{C} = 0 \\ \boldsymbol{J} \cdot \boldsymbol{n} = J^* \end{cases}$	$\begin{cases} \nabla \cdot \boldsymbol{q} + Q(d) \leq 0 \\ \boldsymbol{q} \cdot \boldsymbol{n}_{\mathcal{B}} \geq 0 \end{cases}$
Constitutive relations	$\begin{cases} \boldsymbol{\sigma} = \omega(d, C)\mathbb{E}_0 : \boldsymbol{\epsilon} \\ Y = -\omega'(d, C)\bar{Y} \end{cases}$	$\begin{cases} \boldsymbol{J} = -\dfrac{DC}{RT}\nabla\mu \\ \mu = \mu_0 + RT \ln C - V_H \sigma_H \end{cases}$	$\begin{cases} \boldsymbol{q} = \dfrac{2b}{c_\alpha}G_f \cdot \nabla d \\ Q = Y - \dfrac{G_f}{c_\alpha b}\alpha'(d) \end{cases}$
Dirichlet bcs	$\boldsymbol{u} = \boldsymbol{u}^*$ on $\partial\Omega_u$	$C = C^*$ on $\partial\Omega_C$	$d = d^*$ on $\partial\Omega_d$
Initial conditions	NA	$C(\boldsymbol{x}, 0) = C_0$	NA

[a]The conditions $\dot{d} \geq 0$ and $d \in [0, 1]$ have to be fulfilled.

Box II. The phase-field regularized cohesive zone model (PF-CZM) for hydrogen assisted cracking.

of the displacements, damage and hydrogen concentration. In order to resolve the gradient of the hydrostatic stress, quadratic elements, e.g., 8-node quadrilateral Q8, is preferred for the displacement and concentration fields, while piece-wise linear or bilinear (Q4) elements is used for the damage field such that the approximation is always non-negative. The semi-discrete equation involving the transient term $\dot{C}$ is temporally discretized by the backward Euler scheme. The resulting system of algebraic nonlinear equations are then solved by the alternate minimization solver [29,52]. That is, the whole problem is decomposed into the coupled displacement–hydrogen sub-problem and the damage sub-problem, both of which are solved by Newton-like methods. For the latter, the damage boundedness $d(\boldsymbol{x}, T) \in [0, 1]$ and irreversibility $\dot{d}(\boldsymbol{x}, T) \geq 0$ can be dealt with by the bound-constrained optimization solver [43,66,67]. The numerical aspect will be addressed in details elsewhere.

4. Numerical experiments

In this section, we present several numerical examples to validate the presented models for HAC, including:

- Uniaxial traction of a softening bar with a stationary uniform concentration. This example aims to verify the hydrogen-dependent softening laws without solving the hydrogen diffusion equation.
- Single-edge notched plate with and without presence of hydrogen. Being a popular benchmark, this example involves coupled displacement–hydrogen–damage analyses of a single-edge notched plate. It serves as a simple benchmark test to investigate the influence of hydrogen on fracture.
- Crack growth from corrosion pits. This is a more complex example aiming to demonstrate the performances of the models with distinct HEDE mechanisms. The influence of pit location is also investigated.

The linear softening curve $(2.2)_1$ and the hydrogen degradation function (3.15) are used in all examples. Unless it is explicitly specified as in Section 4.1, we assume an iron-based material and consequently adopt a hydrogen damage coefficient $\chi = 0.89$. All the examples are simulated by feFRAC — our in-house FE code based on the open-source library jive.[2] Interested readers can refer to Nguyen et al. [68] for a description of the computer implementation of a similar poroelasticity model and to Wu et al. [54] for the computational aspects of PFMs. Finite element meshes are generated using Gmsh [69] and visualization is performed in Paraview.

4.1. Uniaxial traction of a softening bar with a uniform hydrogen concentration

In this example we consider a bar of length $L = 200$ mm under uniaxial traction. Unit height and unit out-of-plane thickness are assumed. As shown in Fig. 4, the left edge of the bar is fixed, while the right edge is stretched by a monotonically increasing displacement. The Dirichlet boundary condition $d = 0$ is imposed on both edges of the bar such that the crack can form at any interior position as shown in Fig. 5.

---

[2] Jive is an open source C++ library for solving PDEs using numerical methods. Its webpage is http://www.jem-jive.com.
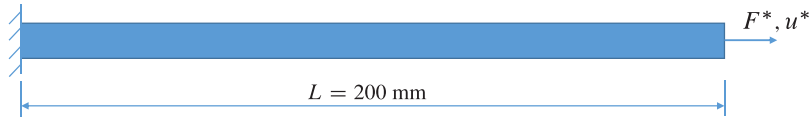
Fig. 4. Uniaxial traction of a softening bar: Geometry, loading and boundary conditions.
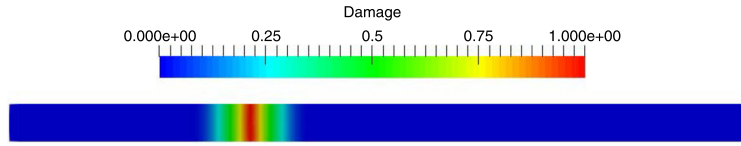
Fig. 5. Uniaxial traction of a softening bar: Typical damage profile.
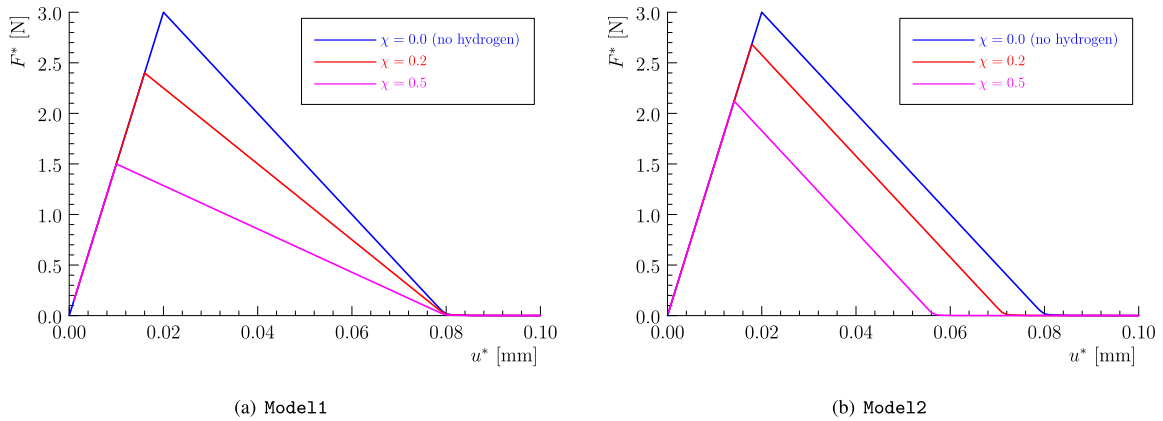

(a) `Model1`   (b) `Model2`

Fig. 6. Uniaxial traction of a softening bar with a uniform hydrogen concentration. The degradation function $\phi(\theta) = 1 - \chi\theta$ with a uniformly distributed hydrogen coverage $\theta = 1.0$ is assumed in the bar.

The following material properties are assumed: Young's modulus $E_0 = 3.0 \times 10^4$ MPa, Poisson's ratio $\nu_0 = 0.2$, the fracture energy $G_{f0} = 0.12$ N/mm and the failure strength $f_{t0} = 3.0$ MPa. As our objective here is to verify the hydrogen-dependent linear softening law, the length scale parameter is taken as $b = 10$ mm, with the mesh size of the adopted Q4 element being $h = 0.01$ mm.

The same example with no hydrogen was first considered in [41]. Herein a hypothetical value of $\theta = 1.0$ is assigned to the hydrogen coverage at every points in the bar (i.e., no diffusion in this case). The hydrogen-dependent degradation function (3.15) with $\chi = 0.2$ and $\chi = 0.5$ is considered. We compare the numerical load–displacement responses against those given by the analytical solution, cf. Fig. 3.

The numerical results given in Fig. 6 validate the proposed hydrogen-dependent softening laws. Regarding `Model1` the failure strength is half of the initial value, i.e., 1.5 MPa for $\chi = 0.5$, resulting in a peak load of 1.5 N; for $\chi = 0.2$ one gets a reduced strength 2.4 MPa and the numerical peak load is 2.4 N. As far as `Model2` is concerned one gets the peak load 2.12 N for $\chi = 0.5$ and 2.68 N for $\chi = 0.2$, respectively. As expected, the limit displacements with vanishing load capacity remain unchanged for `Model1` whereas for `Model2` they reduce as the failure strength, such that the same fracture energy is predicted for an identical hydrogen coverage. In all cases, the hydrogen-dependent linear softening laws are reproduced.

4.2. Single-edge notched plate with hydrogen diffusion

Let us now consider a single-edge notched plate under tension. As shown in Fig. 7, it is a square plate of length 1 mm. A straight horizontal notch of length 0.5 mm is introduced at the mid-height of the left edge. The bottom edge is fixed, while a vertical displacement is applied to the top edge. Being a popular benchmark test verifying
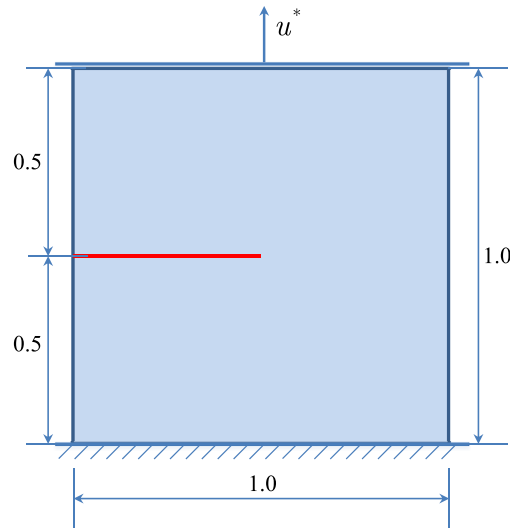
Fig. 7. Single-edge notched plate: Geometry (unit of length: mm), boundary and loading conditions.

phase-field models for brittle fracture [32,53,59], this example is revisited here as in [56] to incorporate the hydrogen effect.

The material mechanical parameters are taken from [32], i.e., Young's modulus $E_0 = 2.1 \times 10^5$ MPa, Poisson's ratio $\nu_0 = 0.3$, the fracture toughness $G_{f0} = 2.7$ N/mm and the failure strength $f_{t0} = 2445.42$ MPa. As in [56], the hydrogen diffusivity is taken as $D = 0.0127$ mm^2/s. A constant concentration C^* is prescribed to all external boundaries (including the crack faces), and an initial uniform distribution of concentration $C_0(\boldsymbol{x}) = C^*$ is assumed (in the transient analysis). The applied displacement rate is 10^{-9} mm/s for a total time $t = 10^7$ seconds. In the numerical simulations, we have used a constant displacement increment $\Delta u^* = 10^{-6}$ mm with the time increment $\Delta t = 10^3$ s.

In order to accurately approximate the gradient of the hydrostatic stress, the eight-node quadratic element (Q8) with reduced integration (2 × 2 Gauss quadrature points) is used in the displacement–hydrogen sub-problem. Comparatively, for the damage sub-problem only the corner nodes of Q8 elements are considered and hence it behaves like four-node bilinear element with full integration scheme (Q4). Hereafter the Q8 element refers to the eight-node quadratic element for the displacement–hydrogen sub-problem and four-node bilinear one in the damage sub-problem. In the simulations, a plane strain state is assumed and the mesh size is $h = 0.001$ mm (about 148,000 Q8 elements) within the damage sub-domain encompassing the crack path.

This section is organized as follows. The length scale sensitivity is addressed in Section 4.2.1. Section 4.2.2 presents a comparison between Model1 and Model2 for HAC. And finally, temporal evolution of the hydrostatic stress, hydrogen concentration and damage is discussed in Section 4.2.3 with respect to Model1.

4.2.1. Length scale sensitivity analysis

In order to study the length scale sensitivity of the proposed PF-CZM for HAC, we consider both Model1 and Model2 using two length scale parameters, i.e., $b = 0.010$ mm and $b = 0.005$ mm, respectively.

For the case with no hydrogen, the predicted curves of vertical force *versus* vertical displacement are shown in Fig. 8, exhibiting no sensitivity to the length scale as reported in our previous work [32].

In the presence of hydrogen concentration, Figs. 9 and 10 depict the global responses given by Model1 and Model2, respectively. As can be seen, *the global responses are insensitive to the incorporated length scale*. This fact is consistent with the extensive numerical examples reported in our previous work for purely mechanical problems [32,41–43,46,54]; see also Fig. 8.
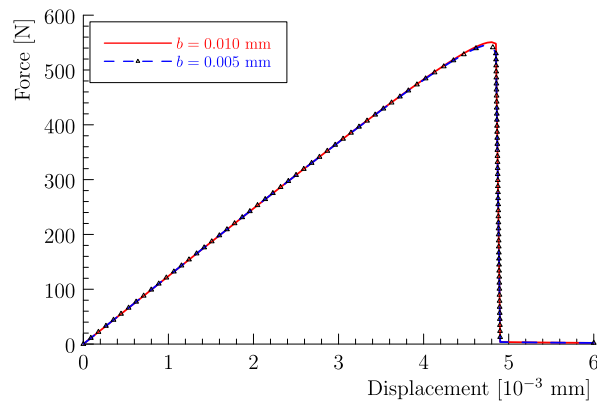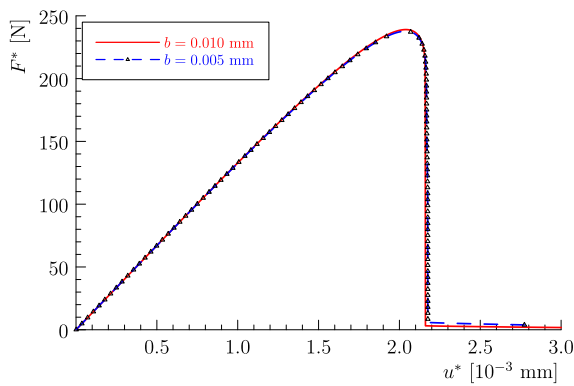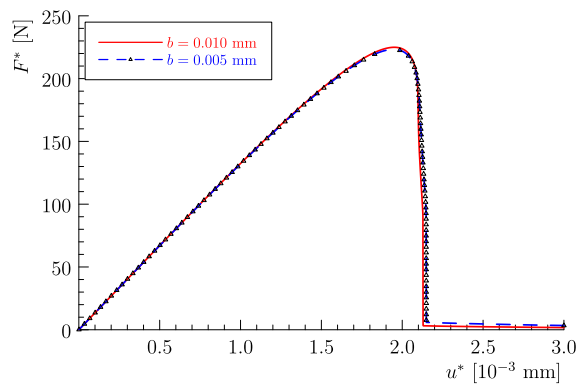
Fig. 8. Single-edge notched plate: Vertical force *versus* vertical displacement for various length scale parameters (with no hydrogen).
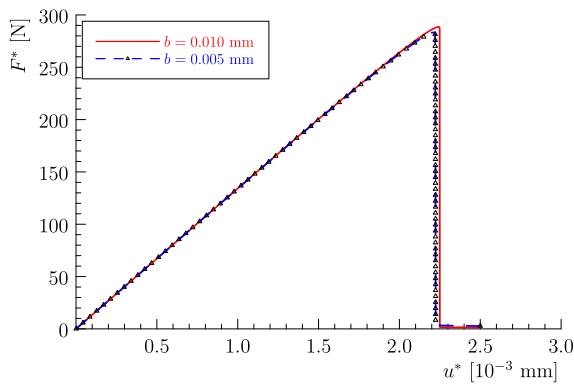

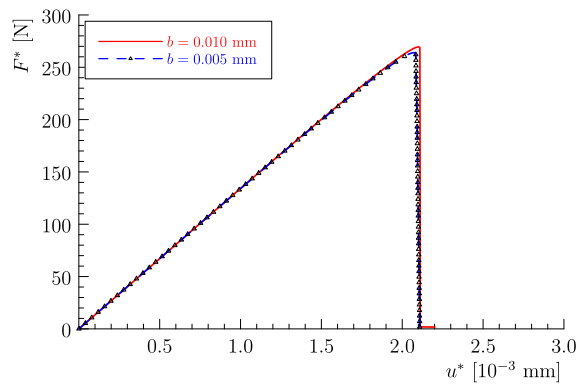(a) Steady analysis for a uniform concentration $C = 0.5$ wt. ppm

(b) Transient analysis for $C^* = 0.5$ wt. ppm

Fig. 9. Single-edge notched plate: Vertical force *versus* vertical displacement for various length scale parameters (`Model1`).
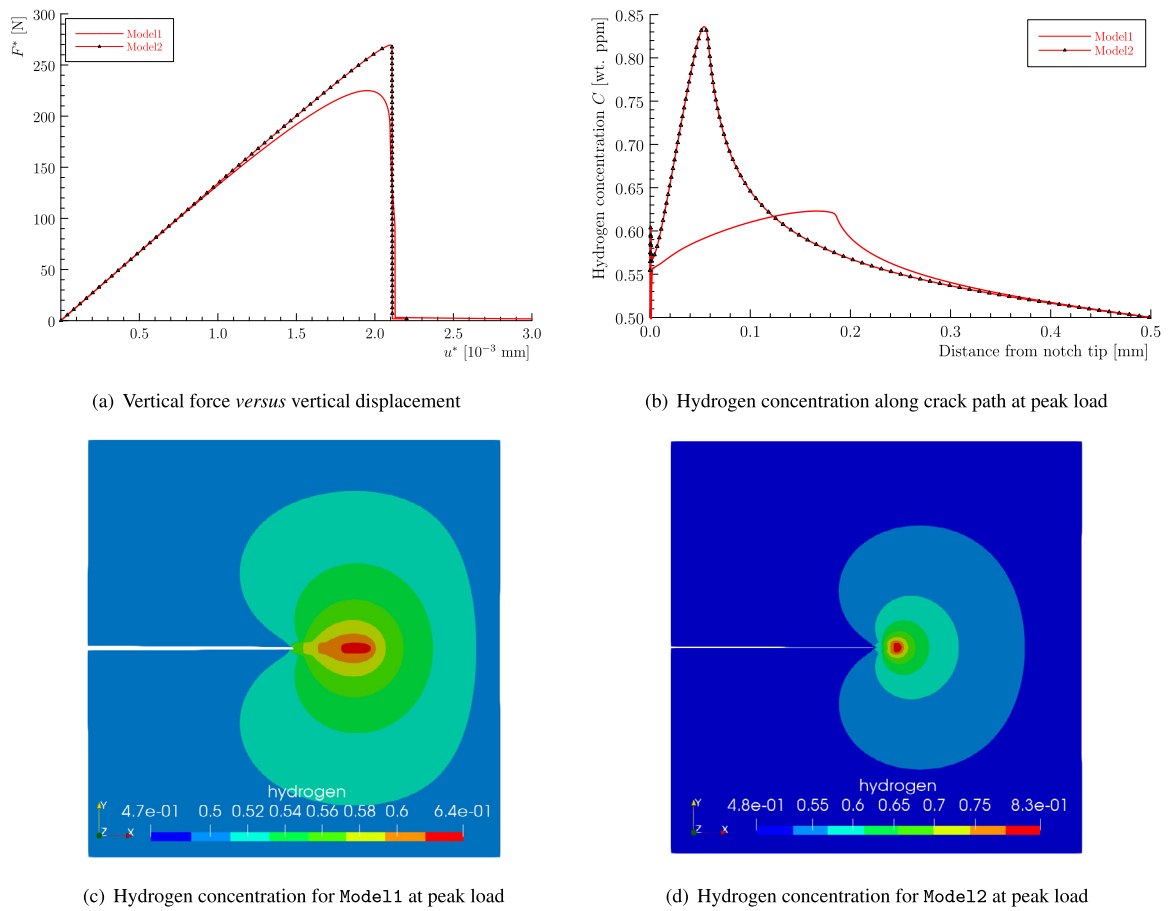

(a) Steady analysis for a uniform concentration $C = 0.5$ wt. ppm

(b) Transient analysis for $C^* = 0.5$ wt. ppm

Fig. 10. Single-edge notched plate: Vertical force *versus* vertical displacement for various length scale parameters (`Model2`).

(a) Vertical force *versus* vertical displacement

(b) Hydrogen concentration along crack path at peak load

(c) Hydrogen concentration for `Model1` at peak load

(d) Hydrogen concentration for `Model2` at peak load

Fig. 11. Single-edge notched plate: Results given from `Model1` and `Model2`.

4.2.2. Comparison between `Model1` and `Model2`

In order to compare `Model1` against `Model2`, we consider a transient state of concentration with $C^* = 0.5$ wt. ppm. As the global responses are insensitive to the length scale parameter, only the results given from $b = 0.010$ mm and $h = 0.001$ mm are presented.

As can be seen from the results shown in Fig. 11(a), in presence of hydrogen concentration the global response predicted by `Model1` is more ductile than that by `Model2`. This is because in the former Irwin's internal length l_{ch} becomes larger with increasing hydrogen concentration, while it is unaffected in the latter. Moreover, as the fracture energy is less reduced by $\sqrt{\phi(\theta)}$, the peak load predicted by `Model2` is larger than `Model1`.

Fig. 11(b) presents the variation of the hydrogen concentration along the crack path at peak load. Due to the distinct HEDE mechanisms, it is not surprising that the distribution of the hydrogen concentration exhibits large discrepancies for these two models. As shown in Figs. 11(c) and 11(d), the more brittle the material is, the larger variation the hydrogen concentration exhibits.

4.2.3. Evolution of hydrogen concentration and damage (`Model1`)

Evolution of the hydrogen concentration and damage predicted by `Model1` is now discussed, again regarding the transient state of hydrogen concentration $C^* = 0.5$ wt. ppm. Four typical instants, from damage nucleation (instant *a*) to final failure (instant *d*), shown in Fig. 13, are considered.

Fig. 12 presents the temporal evolution of the hydrostatic stress (left), hydrogen concentration (middle) and damage (right) given by `Model1` with $b = 0.01$ mm and $h = 0.001$ mm. As can be seen, the hydrostatic stress and hydrogen concentration always attain their maximum values around the notch tip.
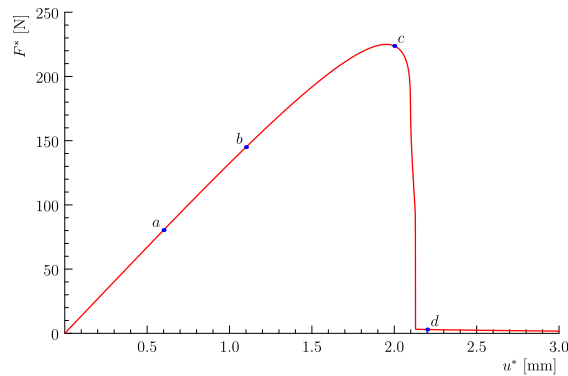
Fig. 12. Single-edge notched plate: Evolution of hydrostatic stress, hydrogen concentration and damage given by `Model1`.

4.3. Crack growth from corrosion pits

Fracture of metallic pipelines often nucleates from corrosion pits, and is accelerated by hydrogen embrittlement. Martínez-Pañeda et al. [56] presented a plane strain example with complex crack paths due to existing defects. The problem configuration is given in Fig. 14, with $x = x_1 = 25$ mm. In this section we re-consider this example using both `Model1` and `Model2` for HAC. However, the corrosion pits are modeled in this work by the finite element mesh rather than by the damage boundary conditions as in [56].

The material parameters are taken unaltered from [56]: Young's modulus $E_0 = 2.0 \times 10^5$ MPa, Poisson's ratio $\nu_0 = 0.3$, the failure strength $f_{t0} = 1778.78$ MPa, the fracture energy $G_{f0} = 90$ N/mm, and the hydrogen diffusivity $D = 1.0 \times 10^{-8}$ mm^2/s (corresponding to that of fcc iron at room temperature). A constant concentration $C^* = 1.0$ wt. ppm is prescribed to all external boundaries (including the corrosion pits), and an initial uniform distribution of concentration $C_0(x) = C^* = 1.0$ wt. ppm is assumed throughout the specimen. As no hydrogen diffusion occurs in this example for such a small diffusivity, the bilinear quadrilateral Q4 element is adopted in the simulations. The load is applied via an imposed displacement u^* with the loading rate 0.0416×10^{-3} mm/s.

This section is organized as follows. The length scale sensitivity is studied in Section 4.3.1. The numerical results given by `Model1` and `Model2` are compared in Section 4.3.2. Evolution of damage with and without hydrogen concentration is discussed in Section 4.3.3. And finally, Section 4.3.4 addresses the effect of corrosion pit location.

4.3.1. Mesh size and length scale sensitivity analysis

In order to study the effect of the length scale parameter, two different values, i.e., $b = 0.4$ mm and $b = 0.2$ mm, are considered. The corresponding mesh sizes within the damage sub-domain are taken as $h = b/5$, i.e., $h = 0.08$ mm (around 70,000 Q4 elements) for $b = 0.4$ mm and $h = 0.04$ mm (about 295,000 Q4 elements) for $b = 0.2$ mm.

For the case with no hydrogen concentration, the predicted damage profiles are shown in Figs. 15(a) and 15(b), respectively. Though the damage bandwidth varies, the crack pattern is not affected by the incorporated length scale. Moreover, it can be seen from Fig. 15 that the global responses given by `Model1` and `Model2` are both independent of the mesh size and the length scale parameter. The above results confirm those conclusions drawn from our previous work on purely mechanical problems [32,41–43].

For `Model1` with hydrogen concentration $C^* = 1.0$ wt. ppm, though the damage bandwidth is proportional to the length scale parameter, the predicted crack patterns are not affected by it; see Figs. 16(a) and 16(b). In particular, the primary crack is similar to that with no hydrogen concentration, though in the former there is a secondary crack nucleating at the top of the bottom corrosion pit. As expected, the global responses shown in Fig. 16(c) depend on neither the mesh size nor the length scale parameter.

Similarly, as far as `Model2` is concerned, despite the different damage bandwidths the crack pattern and the global responses shown in Fig. 17 are independent of the length scale parameter. Remarkably, as Irwin's length scale l_{ch} does not change in `Model2`, the predicted crack pattern is almost identical to that for the case with no hydrogen concentration, though the peak load is significantly lower, cf. Fig. 15.
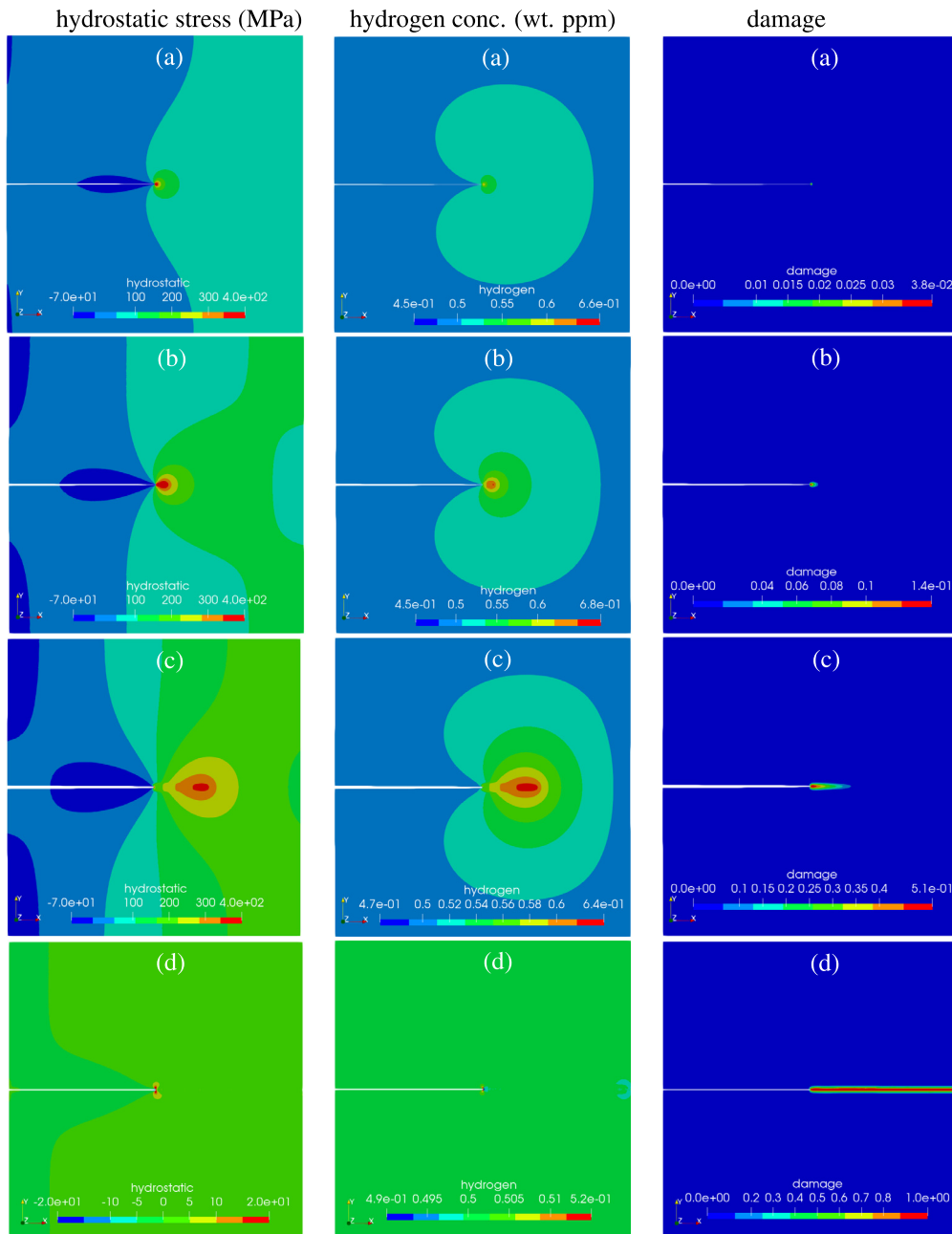
Fig. 13. Single-edge notched plate: Vertical force *versus* vertical displacement given by `Model1` for $C^* = 0.5$ wt. ppm.

4.3.2. Comparison between `Model1` and `Model2`

Fig. 18(a) compares the global responses predicted from `Model1` and `Model2` for the hydrogen concentration $C^* = 1.0$ wt. ppm, in which the length scale parameter $b = 0.4$ mm is used in both models. As can be seen, the peak load predicted by `Model2` is higher than that by `Model1` due to the less degradation of the fracture energy in the former, i.e., $\sqrt{\phi(\theta)}$ *versus* $\phi(\theta)$. Moreover, as we mentioned before, the curve of applied force *versus* displacement predicted by `Model2` resembles that by PF-CZM with no hydrogen, since the presence of hydrogen does not change Irwin's internal length l_{ch} that measures brittleness of the material.
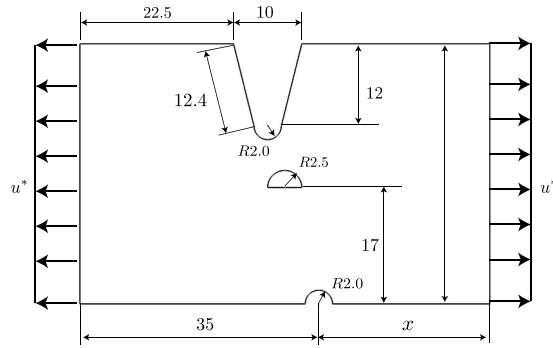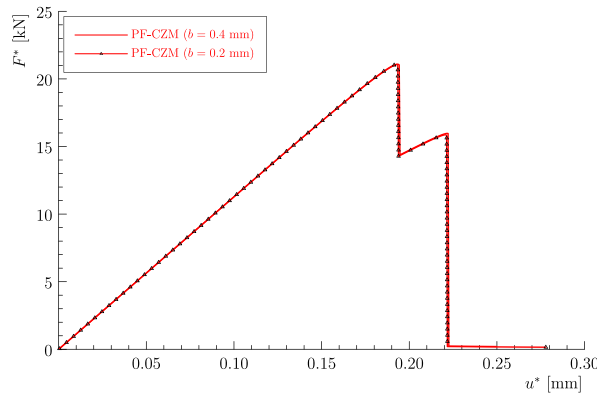
Fig. 14. Corrosion pits problem: geometry (unit of dimension: mm) and loading conditions.
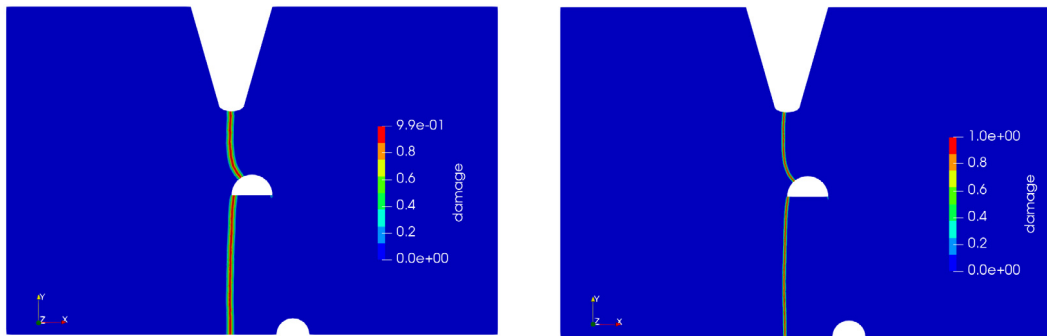
(a) Crack pattern for $b = 0.4$ mm

(b) Crack pattern for $b = 0.2$ mm

(c) Applied force *versus* displacement

Fig. 15. Corrosion pits problem: Numerical results for various mesh sizes and length scale parameters ($C^* = 0.0$ wt. ppm).

Comparatively, the global response given by Model1 is much more ductile in the presence of hydrogen, exhibiting the typical behavior of cohesive fracture rather than the original brittle one. In particular, the curve of applied force *versus* displacement is smooth and the second peak load due to crack arresting of the middle pit vanishes. This is rational since Irwin's internal length l_{ch} becomes larger for Model1 with a constant ratio G_f/f_t. As shown in Fig. 18(b), Irwin's internal length varies from $l_{ch} = 5.7$ mm for $C^* = 0.0$ wt. ppm (no hydrogen) to $l_{ch} = 28.8$ mm for $C^* = 1.0$ wt. ppm, resulting in a global response progressively from brittle behavior to cohesive one.
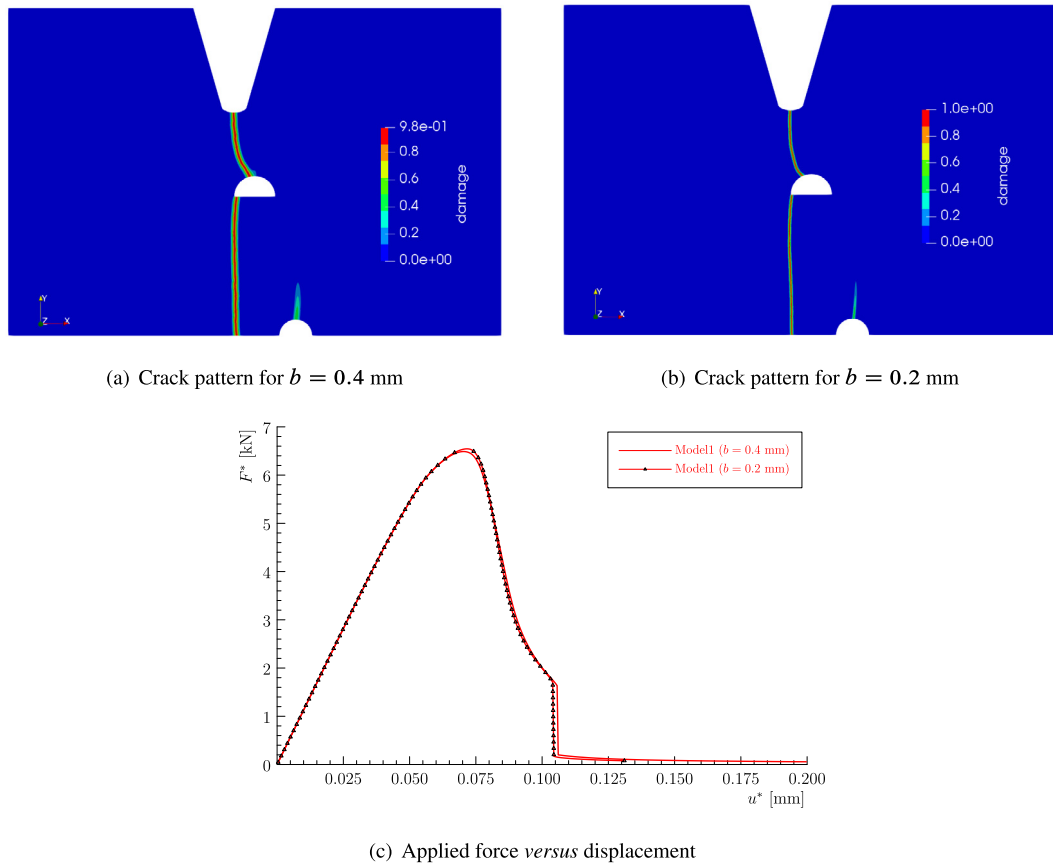
(a) Crack pattern for $b = 0.4$ mm   (b) Crack pattern for $b = 0.2$ mm

(c) Applied force *versus* displacement

Fig. 16. Corrosion pits problem: Numerical results for various mesh sizes and length scale parameters (Model1 with $C^* = 1.0$ wt. ppm).

4.3.3. Damage evolution with/without hydrogen

The effects of hydrogen concentration on damage evolution are now discussed, also regarding the results given from the length scale parameter $b = 0.4$ mm.

As shown in Table 1, for the case with no hydrogen ($C^* = 0.0$ wt. ppm) the cracking process is quite brittle: at about $u^* = 0.19$ mm, the first crack nucleates at the top pit and propagates in a brittle manner towards the middle pit, resulting in the first load drop. About $u^* = 0.22$ mm a second crack nucleates at the middle pit and propagates vertically downwards to the bottom edge, leading to final failure of the specimen.

As we discussed in the previous section, for the case with hydrogen ($C^* = 1.0$ wt. ppm), the global responses and damage evolution given by Model1 and Model2 are quite different; see Table 2.

Model1 exhibits typical cohesive behavior and the global response is quite smooth before final failure. The first crack nucleates at the top pit (instant *a*) and then the second one initiates at the top surface of the middle pit. During this time the load continues increasing until it reaches the peak point (instant *b*) upon which these two cracks almost merge. Subsequently, another new crack nucleates at the bottom surface of the middle pit and propagates downward rapidly to the bottom edge of the specimen (instant *c*), leading to final failure (instant *d*). During this period, a fourth crack initiates at the bottom pit, but it propagates very slowly and does not contribute too much to the final failure.

Comparatively, Model2 predicts almost the same brittle response as the case with no hydrogen. The first crack nucleates nearly around the peak load (instant *a*). It propagates rapidly to the middle pit, leading to a abruptly load drop (instant *b*). And then the first crack is arrested until the load increases to a local peak (instant *c*) when a second crack nucleates at the corner of the middle pit. Subsequently, the second crack propagates downwards rapidly and finally reaches the bottom edge of the specimen, resulting in the eventual failure (instant *d*).
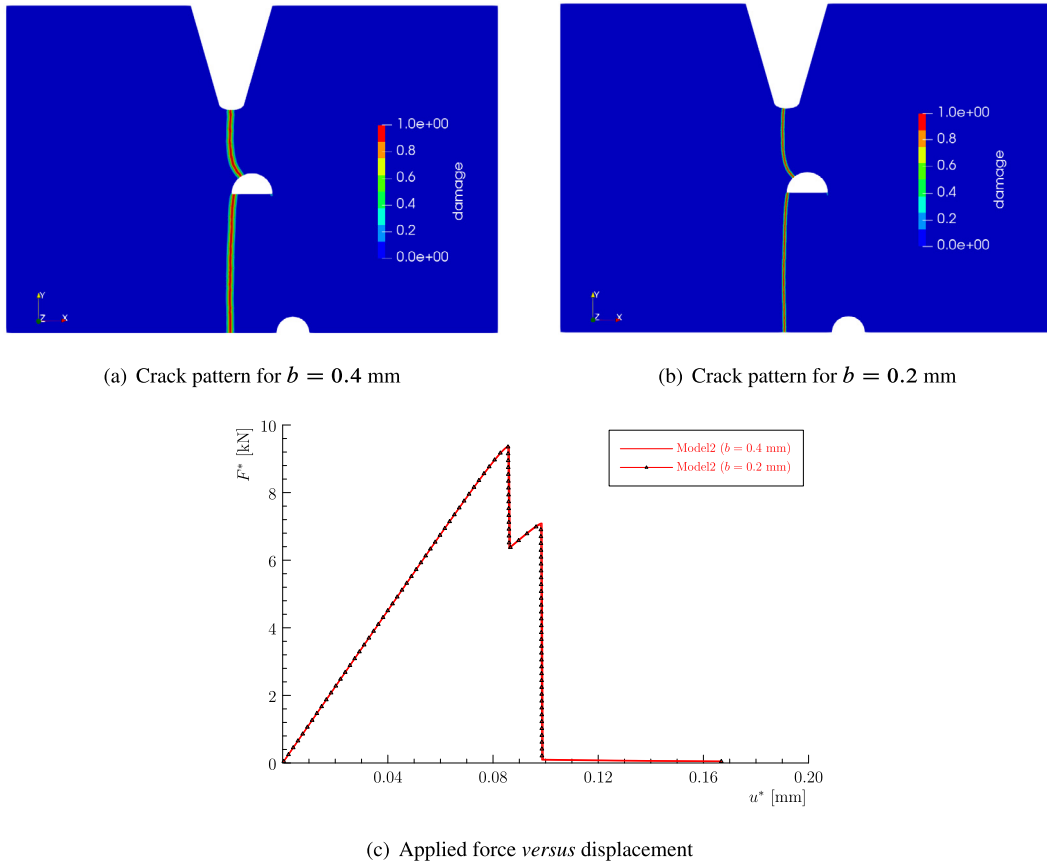
(a) Crack pattern for $b = 0.4$ mm

(b) Crack pattern for $b = 0.2$ mm

(c) Applied force *versus* displacement

Fig. 17. Corrosion pits problem: Numerical results for various mesh sizes and length scale parameters (`Model2` with $C^* = 1.0$ wt. ppm).
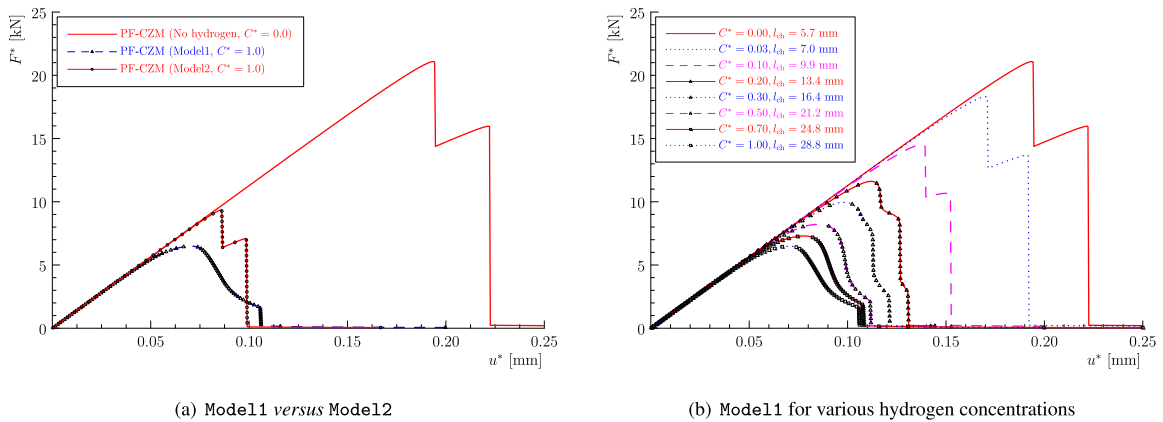

(a) `Model1` *versus* `Model2`

(b) `Model1` for various hydrogen concentrations

Fig. 18. Corrosion pits problem: Applied force *versus* displacement curves for different models and various hydrogen concentrations.

4.3.4. Effect of corrosion pit location

As it is found in [56] that the standard PFM [29,59] is sensitive to the location of the bottom corrosion pit, we finally study the effect of pit location on the crack pattern and global response. To this end, two geometries with $x = x_1 = 25$ mm and $x = x_2 = 26$ mm, respectively, are compared. Again, only those results given from the length scale parameter $b = 0.4$ mm are tabulated in Table 3.

Table 1
Corrosion pits problem: Applied force *versus* displacement curve (top) and damage evolution (bottom) for $C^* = 0.0$ wt.ppm.
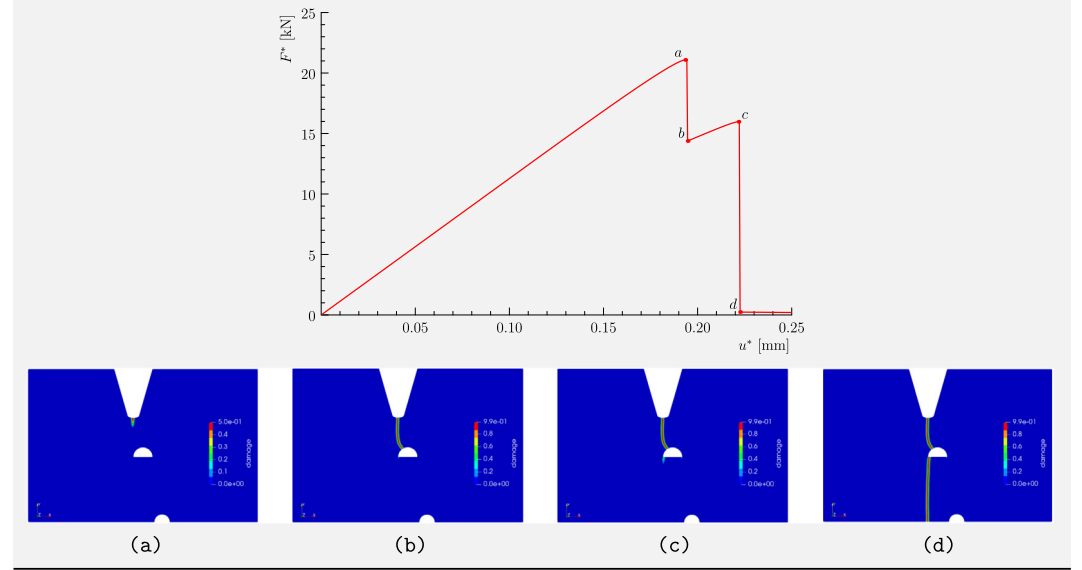

Table 2
Corrosion pits problem: Applied force *versus* displacement curves (top) and damage evolution (bottom) for $C^* = 1.0$ wt.ppm.
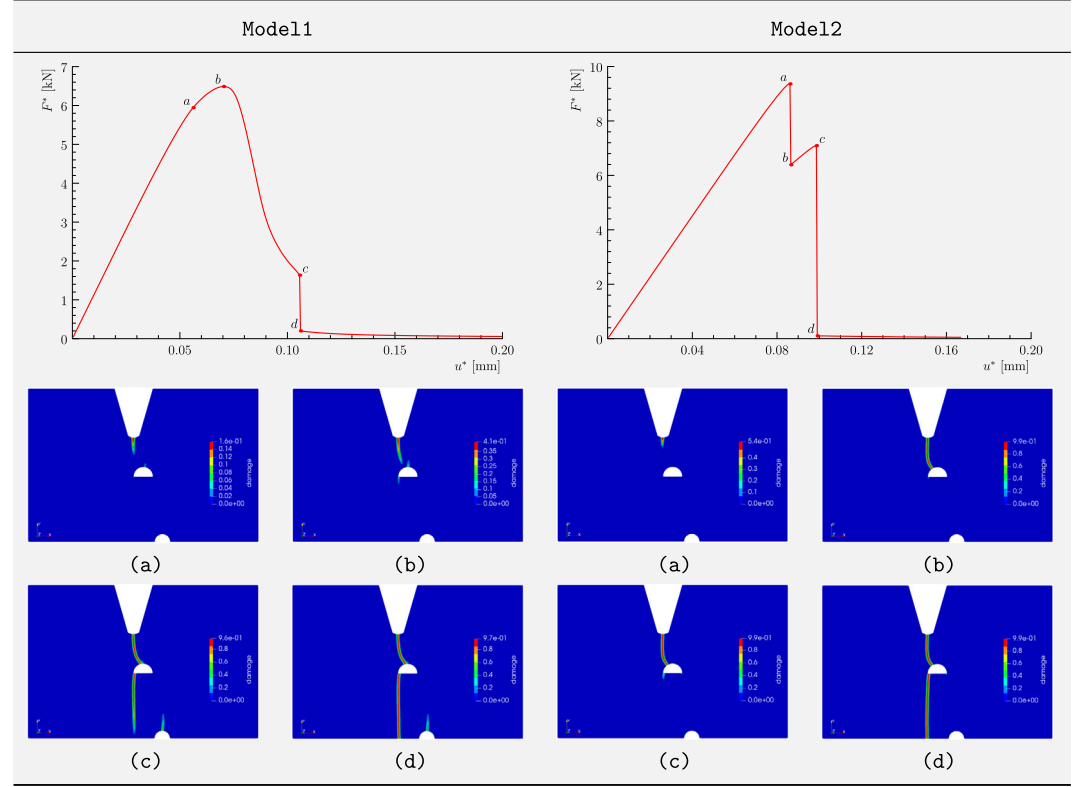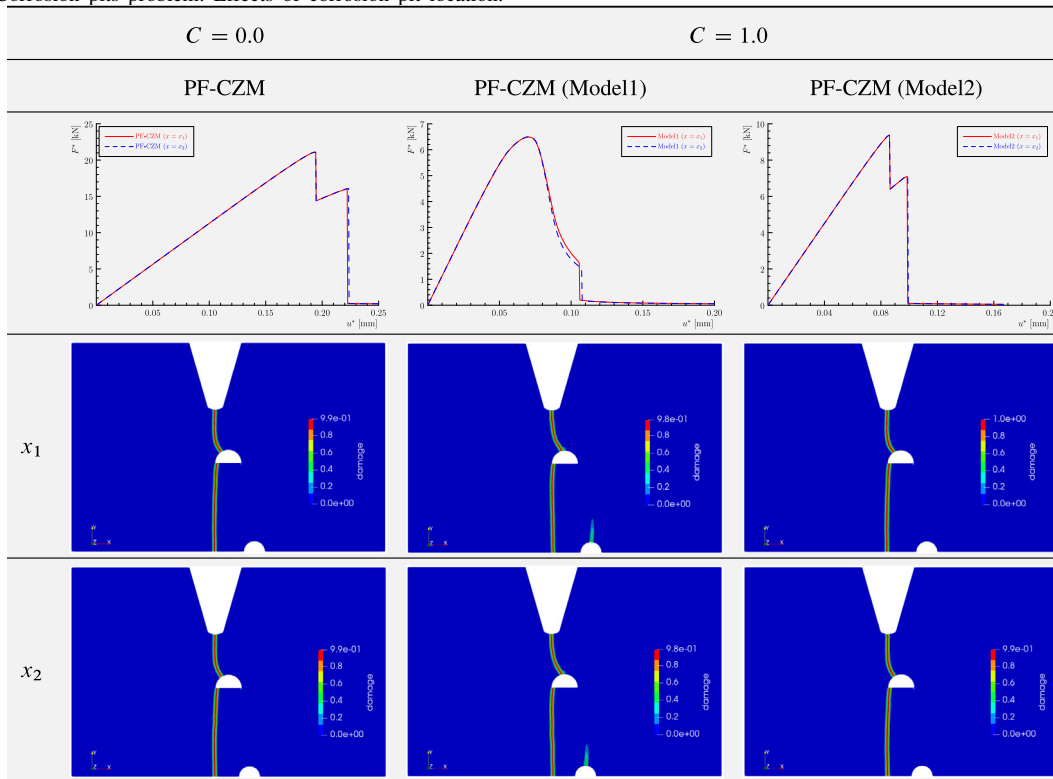
Table 3
Corrosion pits problem: Effects of corrosion pit location.

As can be seen, no matter whether the hydrogen is present or not, the location of the bottom corrosion pit has negligible effects on the global response and crack pattern for the two geometries of interest. Even for Model1, the secondary crack nucleating at the bottom pit does not interfere in propagation of the primary one, probably due to the narrow and finite support of the damage band in the PF-CZM. However, this is not the case for the standard PFM in which the damage band is of infinite support such that the secondary crack finally merges with the primary one if the bottom pit moves closer to the centroid of the bottom edge.

5. Conclusions

In this work we have extended our previous phase-field regularized cohesive zone model (PF-CZM) for purely mechanical problem to deal with hydrogen assisted cracking (HAC). Two distinct hydrogen enhanced decohesion (HEDE) mechanisms are considered by coupling mechanical–diffusion responses and introducing various implicitly defined (via the crack phase-field) hydrogen-dependent softening laws. The respective performances of the resulting models are tested and compared against several benchmark examples. From the numerical study, it is found that even if the hydrogen is present, Model1 and Model2, are both insensitive to the incorporated length scale parameter, thus preserving the Γ-convergence of phase-field models [52]. More importantly, the crack pattern and global response given by the PF-CZM are consistent in all cases, making it a promising tool in the modeling of hydrogen assisted cracking and other similar coupled multi-physics problems.

So far only the HEDE mechanism has been accounted for in this work. Another mechanism responsible for HAC, i.e., the hydrogen enhanced localized plasticity (HELP), will be addressed later. Moreover, in this work only the PF-CZM with hybrid formulation is considered. It will be extended to incorporate the variationally consistent split [70,71] such that more complex other than tension-dominant problems can be dealt with.

Acknowledgments

References

[1] L.E. Malvern, Introduction to the Mechanics of a Continuous Medium, Prentice-Hall International, Englewood Cliffs, New Jersey, 1969.

[2] S.L. Lee, D.J. Unger, A decohesion model of hydrogen assisted cracking, Eng. Fract. Mech. 31 (4) (1988) 647–660.

[3] P. Sofronis, R. McMeeking, Numerical analysis of hydrogen transport near a blunting crack tip, J. Mech. Phys. Solids 37 (3) (1989) 317–350.

[4] S. Serebrinsky, E. Carter, M. Ortiz, A quantum-mechanically informed continuum model of hydrogen embrittlement, J. Mech. Phys. Solids 52 (10) (2004) 2403–2430.

[5] A. Díaz, J. Alegre, I. Cuesta, Coupled hydrogen diffusion simulation using a heat transfer analogy, Int. J. Mech. Sci. 115 (2016) 360–369.

[6] A. Díaz, J. Alegre, I. Cuesta, A review on diffusion modelling in hydrogen related failures of metals, Eng. Fail. Anal. 66 (2016) 577–595.

[7] H.K. Birnbaum, P. Sofronis, Hydrogen-enhanced localized plasticity—a mechanism for hydrogen-related fracture, Mater. Sci. Eng. A 176 (1–2) (1994) 191–202.

[8] E. Martínez-Pañeda, S. del Busto, C.F. Niordson, C. Betegón, Strain gradient plasticity modeling of hydrogen diffusion to the crack tip, Int. J. Hydrogen Energy 41 (24) (2016) 10265–10274.

[9] R. Falkenberg, A phase field approach to fracture with mass transport extension for the simulation of environmentally-assisted cracking, in: Key Engineering Materials. Vol. 754, Trans Tech Publ, 2017, pp. 153–156.

[10] G.I. Barenblatt, The formation of equilibrium cracks during brittle fracture. general ideas and hypotheses. axially-symmetric cracks, J. Appl. Math. Mech. 23 (1959) 622–636.

[11] I. Scheider, M. Pfuff, W. Dietzel, Simulation of hydrogen assisted stress corrosion cracking using the cohesive model, Eng. Fract. Mech. 75 (15) (2008) 4283–4291.

[12] V. Olden, C. Thaulow, R. Johnsen, E. Østby, T. Berstad, Influence of hydrogen from cathodic protection on the fracture susceptibility of 25% cr duplex stainless steel–constant load sent testing and fe-modelling using hydrogen influenced cohesive zone elements, Eng. Fract. Mech. 76 (7) (2009) 827–844.

[13] C. Moriconi, G. Hénaff, D. Halm, Cohesive zone modeling of fatigue crack propagation assisted by gaseous hydrogen in metals, Int. J. Fatigue 68 (2014) 56–66.

[14] A. Alvaro, I.T. Jensen, N. Kheradmand, O. Løvvik, V. Olden, Hydrogen embrittlement in nickel, visited by first principles modeling, cohesive zone simulation and nanomechanical testing, Int. J. Hydrogen Energy 40 (47) (2015) 16892–16900.

[15] X. Xu, A. Needleman, Numerical simulations of fast crack growth in brittle solids, J. Mech. Phys. Solids 42 (9) (1994).

[16] V.P. Nguyen, C.T. Nguyen, S. Bordas, A. Heidapour, Modelling interfacial cracking with non-matching cohesive interface elements, Comput. Mech. 58 (5) (2016) 731–746.

[17] V.P. Nguyen, Discontinuous Galerkin/Extrinsic cohesive zone modeling: implementation caveats and applications in computational fracture mechanics, Eng. Fract. Mech. 128 (2014) 37–68.

[18] J. Simó, J. Oliver, F. Armero, An analysis of strong discontinuities induced by strain-softening in rate-independent inelastic solids, Comput. Mech. 12 (1993) 277–296.

[19] J. Oliver, Modeling strong discontinuities in solid mechanics via strain softening constitutive equations. part i: fundamentals; part ii: Numerical simulation, Int. J. Numer. Methods Eng. 39 (1996) 3575–3600, 3601–3623.

[20] N. Moës, J. Dolbow, T. Belytschko, A finite element method for crack growth without remeshing, Internat. J. Numer. Methods Engrg. 46 (1) (1999) 133–150.

[21] G.N. Wells, L.J. Sluys, A new method for modelling cohesive cracks using finite elements, Internat. J. Numer. Methods Engrg. 50 (12) (2001) 2667–2682.

[22] C. Linder, F. Armero, Finite elements with embedded strong discontinuities for the modeling of failure in solids, Internat. J. Numer. Methods Engrg. 72 (2007) 1391–1433.

[23] J.Y. Wu, F.B. Li, S.L. Xu, Extended embedded finite elements with continuous displacement jumps for the modeling of localized failure in solids, Comput. Methods Appl. Mech. Engrg. 285 (2015) 346–378.

[24] J.Y. Wu, F.B. Li, An improved stable xfem (is-xfem) with a novel enrichment function for the computational modeling of cohesive cracks, Comput. Methods Appl. Mech. Engrg. 295 (2015) 77–107.

[25] Y. Zhang, R. Lackner, M. Zeiml, H. Mang, Strong discontinuity embedded approach with standard sos formulation: Element formulation, energy-based crack-tracking strategy, and validations, Comput. Methods Appl. Mech. Engrg. 287 (2015) 335–366.

[26] L. Poh, G. Sun, Localizing gradient damage model with decreasing interactions, Internat. J. Numer. Methods Engrg. (2016) http://dx.doi.org/10.1002/nme.5364.

[27] Y. Zhang, X. Zhuang, Cracking elements: A self-propagating strong discontinuity embedded approach for quasi-brittle fracture, Finite Elem. Anal. Des. 144 (2018) 84–100.

[28] G. Francfort, J.-J. Marigo, Revisiting brittle fracture as an energy minimization problem, J. Mech. Phys. Solids 46 (8) (1998) 1319–1342.

[29] B. Bourdin, G. Francfort, J.-J. Marigo, Numerical experiments in revisited brittle fracture, J. Mech. Phys. Solids 48 (4) (2000) 797–826.

[30] K.H. Pham, K. Ravi-Chandar, The formation and growth of echelon cracks in brittle materials, Int. J. Fract. 206 (2) (2017) 229–244.

[31] E. Tanné, T. Li, B. Bourdin, J.J. Marigo, C. Maurini, Crack nucleation in variational phase-field models of brittle fracture, J. Mech. Phys. Solids 110 (2018) 80–99.

[32] J.Y. Wu, V.P. Nguyen, A length scale insensitive phase-field damage model for brittle fracture, J. Mech. Phys. Solids 119 (2018) 20–42.

[33] C. Miehe, M. Hofacker, L.-M. Schänzel, F. Aldakheel, Phase field modeling of fracture in multi-physics problems. part ii. coupled brittle-to-ductile failure criteria and crack propagation in thermo-elastic–plastic solids, Comput. Methods Appl. Mech. Engrg. 294 (2015) 486–522.

[34] M. Ambati, R. Kruse, L. De Lorenzis, A phase-field model for ductile fracture at finite strains and its experimental verification, Comput. Mech. 57 (1) (2016) 149–167.

[35] M.J. Borden, T.J. Hughes, C.M. Landis, A. Anvari, I.J. Lee, A phase-field formulation for fracture in ductile materials: Finite deformation balance law derivation, plastic degradation, and stress triaxiality effects, Comput. Methods Appl. Mech. Engrg. 312 (2016) 130–166.

[36] M. Hofacker, C. Miehe, Continuum phase field modeling of dynamic fracture: variational principles and staggered FE implementation, Int. J. Fract. 178 (1) (2012) 113–129.

[37] M.J. Borden, C.V. Verhoosel, M.A. Scott, T.J. Hughes, C.M. Landis, A phase-field description of dynamic brittle fracture, Comput. Methods Appl. Mech. Eng. 217-220 (2012) 77–95.

[38] A. Schlüter, A. Willenbücher, C. Kuhn, R. Müller, Phase field approximation of dynamic brittle fracture, Comput. Mech. 54 (5) (2014) 1141–1161.

[39] T. Li, J.-J. Marigo, D. Guilbaud, S. Potapov, Gradient damage modeling of brittle fracture in an explicit dynamics context, Internat. J. Numer. Methods Engrg. 108 (11) (2016) 1381–1405.

[40] V.P. Nguyen, J.Y. Wu, Modeling dynamic fracture of solids using a phase-field regularized cohesive zone model, Comput. Methods Appl. Mech. Engrg. 340 (2018) 1000–1022.

[41] J.Y. Wu, A unified phase-field theory for the mechanics of damage and quasi-brittle failure in solids, J. Mech. Phys. Solids 103 (2017) 72–99.

[42] J.Y. Wu, A geometrically regularized gradient-damage model with energetic equivalence, Comput. Methods Appl. Mech. Engrg. 328 (2018) 612–637.

[43] J.Y. Wu, Numerical implementation of non-standard phase-field damage models, Comput. Methods Appl. Mech. Engrg. 340 (2018) 767–797.

[44] D.C. Feng, J.Y. Wu, Phase-field regularized cohesize zone model (czm) and size effect of concrete, Eng. Fract. Mech. 197 (2018) 66–79.

[45] J.Y. Wu, J.F. Qiu, V.P. Nguyen, L.J. Zhuang, K.M. Tushar, Computational modeling of localized failure in solids: Xfem vs pf-czm, Comput. Methods Appl. Mech. Engrg. 345 (2019) 618–643.

[46] T.K. Mandal, V.P. Nguyen, A. Heidarpour, Phase field and gradient enhanced damage models for quasi-brittle failure: A numerical comparative study, Eng. Fract. Mech. 207 (2019) 48–67.

[47] C. Miehe, L.-M. Schaenzel, H. Ulmer, Phase field modeling of fracture in multi-physics problems. Part I. balance of crack surface and failure criteria for brittle crack propagation in thermo-elastic solids, Comput. Methods Appl. Mech. Engrg. 294 (2015) 449–485.

[48] T. Wu, L.D. Lorenzis, A phase-field approach to fracture coupled with diffusion, Comput. Methods Appl. Mech. Engrg. 312 (2016) 196–223.

[49] S. Lee, M.F. Wheeler, T. Wick, Pressure and fluid-driven fracture propagation in porous media using an adaptive finite element phase field model, Comput. Methods Appl. Mech. Engrg. 305 (2016) 111–132.

[50] C. Miehe, S. Mauthe, Phase field modeling of fracture in multi-physics problems, Part III. crack driving forces in hydro-poro-elasticity and hydraulic fracturing of fluid-saturated porous media, Comput. Methods Appl. Mech. Engrg. 304 (2016) 619–655.

[51] S. Zhou, X. Zhuang, T. Rabczuk, A phase-field modeling approach of fracture propagation in poroelastic media, Eng. Geol. 240 (2018) 189–203.

[52] B. Bourdin, G. Francfort, J.-J. Marigo, The Variational Approach to Fracture, Springer, Berlin, 2008.

[53] M. Ambati, T. Gerasimov, L. de Lorenzis, A review on phase-field models for brittle fracture and a new fast hybrid formulation, Comput. Mech. 55 (2015) 383–405.

[54] J.Y. Wu, V.P. Nguyen, C.T. Nguyen, D. Sutula, S. Sinaie, S. Bordas, Phase field modeling of fracture, in: Advances in Applied Mechancis: Fracture Mechanics: Recent Developments and Trends Volume 53, 2019, in press.

[55] T.-T. Nguyen, J. Bolivar, J. Rethore, M.-C. Baietto, M. Fregonese, A phase field method for modeling stress corrosion crack propagation in a nickel base alloy, Int. J. Solids Struct. 112 (2017) 65–82.

[56] E. Martínez-Pañeda, A. Golahmar, C.F. Niordson, A phase field formulation for hydrogen assisted cracking, Comput. Methods Appl. Mech. Engrg. 342 (2018) 742–761.

[57] R. Falkenberg, Modelling of environmentally assisted material degradation in the crack phase-field framework, Proc. Inst. Mech. Eng. L (2018) https://doi.org/101177/1464420718761220.

[58] C. Miehe, F. Welschinger, M. Hofacker, Thermodynamically consistent phase-field models of fracture: Variational principles and multi-field FE implementations, Internat. J. Numer. Methods Engrg. 83 (10) (2010) 1273–1311.

[59] C. Miehe, M. Hofacker, F. Welschinger, A phase field model for rate-independent crack propagation: Robust algorithmic implementation based on operator splits, Comput. Methods Appl. Mech. Engrg. 199 (45–48) (2010) 2765–2778.

[60] K. Pham, H. Amor, J.-J. Marigo, C. Maurini, Gradient damage models and their use to approximate brittle fracture, Int. J. Damage Mech. 20 (2011) 618–652.

[61] T.T. Nguyen, J. Yvonnet, M. Bornert, C. Chateau, K. Sab, R. Romani, R. Le Roy, On the choice of parameters in the phase field method for simulating crack initiation with experimental validation, Int. J. Fract. 197 (2) (2016) 213–226.

[62] D.A. Porter, K.E. Easterling, M. Sherif, Phase Transformations in Metals and Alloys, (Revised Reprint), CRC press, 2009.

[63] S. del Busto, C. Betegón, E. Martínez-Pañeda, A cohesive zone framework for environmentally assisted fatigue, Eng. Fract. Mech. 185 (2017) 210–226.

[64] N. Raykar, S. Maiti, R.S. Raman, S. Aryan, Study of hydrogen concentration dependent growth of external annular crack in round tensile specimen using cohesive zone model, Eng. Fract. Mech. 106 (2013) 49–66.

[65] E. Hondros, M. Seah, The theory of grain boundary segregation in terms of surface adsorption analogues, Metall. Trans. A 8 (9) (1977) 1363–1371.

[66] H. Amor, J. Marigo, C. Maurini, Regularized formulation of the variational brittle fracture with unilateral contact: numerical experiments, J. Mech. Phys. Solids 57 (2009) 1209–1229.

[67] P. Farrell, C. Maurini, Linear and nonlinear solvers for variational phase-field models of brittle fracture, Internat. J. Numer. Methods Engrg. 109 (5) (2017) 648–667.

[68] V.P. Nguyen, H. Lian, T. Rabczuk, S. Bordas, Modelling hydraulic fractures in porous media using flow cohesive interface elements, Eng. Geol. 225 (2017) 68–82.

[69] C. Geuzaine, J.-F. Remacle, Gmsh: a three-dimensional finite element mesh generator with built-in pre- and post-processing facilities, Int. J. Numer. Eng. 79 (11) (2009) 1309–1331.

[70] J.Y. Wu, M. Cervera, A novel positive/negative projection in energy norm for the damage modeling of quasi-brittle solids, Int. J. Solids Struct. 139–140 (2018) 250–269.

[71] J.Y. Wu, V.P. Nguyen, H. Zhou, Y. Huang, A variationally consistent phase-field anisotropic damage model for fracture, Comput. Methods Appl. Mech. Engrg. 358 (2020) 112629.